Edinburgh Research Explorer

Multiscale FE Modelling and Design of Composite Laminates Under Impact

Citation for published version:
Martinez-Hergueta, F 2018, Multiscale FE Modelling and Design of Composite Laminates Under Impact. in Reference Module in Materials Science and Materials Engineering.

Link:
Link to publication record in Edinburgh Research Explorer

Document Version:
Publisher's PDF, also known as Version of record

Published In:
Reference Module in Materials Science and Materials Engineering

OPEN ACCESS

8.12 Multiscale FE Modelling and Design of Composite Laminates Under Impact

Diego Garijo, Francisca Martínez, and Cláudio S Lopes, IMDEA Materials Institute, Getafe, Madrid, Spain
Javier Llorca and Carlos González, IMDEA Materials Institute, Getafe, Madrid, Spain and Polytechnic University of Madrid, Madrid, Spain
Jorge L Puente and José A Loya, University Carlos III of Madrid, Leganés, Madrid, Spain
Javier Toral-Vázquez, Vasilis Votsios, and Esteban Martino, Airbus Operations, S.L., Paseo de John Lennon, s/n, Getafe, Madrid, Spain

8.12.1 Introduction

The increasing incorporation of lightweight, high-performance composites into modern structural designs represents a natural step in the optimization roadmap defined to satisfy the demanding needs and regulations of the transport industry nowadays. The outstanding specific mechanical properties of composites make possible stronger, faster, lighter, safer, and greener vehicles. But the full, efficient exploitation of the advantages of composites still tackles challenging tasks, such as the monitoring of structural integrity or the reduction of development costs. In particular, a pursued aim of the engineering community is the eventual replacement of expensive and time-consuming test campaigns by accurate computational predictions of the mechanical behavior and failure of composite materials. In this context, virtual testing[1–3] constitutes a framework of advanced analysis and simulation techniques capable of bridging different length scales by transferring, from one level to the others, relevant information of the properties and failure mechanisms of and between the constituent materials.[4]

Virtual testing strategy is supported by the increased capacity of computational resources available today. Thus, massive finite element (FE) models involving millions of degrees of freedom are the standard, and have already been applied with success – and in assumable CPU times – to reproduce coupon tests[5,6] and in high-fidelity simulations at the small component scale, for example, impacts on panels and subsequent damage tolerance tests.[7] Here, the use of appropriate modeling strategies and correct parameter selection are essential from the point of view of accuracy and numerical efficiency. Otherwise, simulations may result impracticable in terms of computational cost.

In spite of the importance of the numerical implementation, the background and main pillar of virtual testing is the knowledge about the intrinsic nature of the physical phenomena being simulated and the associated response of the material, this is, its constitutive behavior. In this sense, the virtual testing horizon has also boosted the development of analytical and semi empirical models to characterise the damage phenomena that take place in orthotropic media. In particular, the failure and energy absorption mechanisms involved in impact events on fiber reinforced polymer (FRP) laminates – the mesoscale – are well identified in the literature.[8,9] These include indentation, cone formation on the back face of the target, fiber breakage, deformation of primary and secondary yarns, delamination, matrix cracking, shear plugging, and friction during penetration. Some of these mesomechanisms are triggered at the micromechanical scale, and often coupling among them occurs. The resulting structural

response of the impacted composite material becomes highly nonlinear. The dynamic loading generates large deformations, which usually translate into large distortions in the FEs of the discretization. The inertial and strain rate effects during impact depend to a large extent on the time scale of the event, ranging from quasistatic to wave dominated responses. Besides, local (plugging at the impact point) and global (membrane-like) deformations may predominate depending on the impact velocity and the relation of masses between impactor and target[10]. Therefore, from an engineering point of view, features such as the impact regime, i.e., low velocity (LVI) or high velocity (HVI) impact conditions, the shape and impact energy of the projectile and the specific config-uration of the impacted composite target – layup architecture, constituent materials, fixity conditions, etc. – affect to the weight of each mechanism on the final structural response.

In summary, predicting the performance of composite components against external menaces, such as runway debris, una-voidable birds, uncontained engine blade-off fragments, or accidental tool drop – this latter, potential cause of detrimental embedded barely visual impact damage (BVID) – relies on the proper analytical and numerical modeling of multiple coupled physical mechanisms. Both, analytical and numerical treatments, must be conducted in parallel since interdependencies exist between the two approaches. The characterization of damage in composites by means of a generalized material constitutive behavior is based on failure criteria and propagation laws that have been enriched with numerous contributions.[7,11−16] On the other hand, FE modeling of impact on composites must conjugate the implementation of the damage models with a correct discretization of the domain of analysis. And here, the dependence of the impact results on the mesh size is one of the main obstacles faced by researchers today. The original adjustment of the mesh parameter h proposed by Bažant and Oh[17] to preserve the fracture energy in fracture processes driven by strain softening laws was a key achievement in the development of crack modeling in composites. The extension of the mesh regularization to ensure the correct computation of the energy dissipated during delamination with cohesive FEs was detailed by Turon *et al.*[18] Nowadays, investigators are still working on different mesh-regularization strategies, and important efforts are being devoted to the consolidation of mesh-size independent impact predic-tions.[19] Other current trends among the scientific community to simulate HVI impacts on composite parts are the alternative discretizations to the FEs. Recent experiments with the use of meshfree approximations to simulate the targets – the meshfree smoothed particle hydrodynamics technique has been traditionally employed for the modeling of birds and ice fragments – have proven excellent performances, alleviating the problems associated to large deformations and distortions of standard FEs. An example is the work by Raimondo *et al.*[20] on the simulation of ballistic impacts on unidirectional (UD) carbon fibers laminates with the Element Free Galerkin Method (EFGM, Belytschko *et al.*).[21]

The present chapter focuses on the description of computational strategies that can be adopted for the generation of high-fidelity models of impact on composites. The exposition fits within the frame of continuum damage mechanics (CDM) theory and its implementation in explicit FE codes. Unlike other techniques that pose the treatment of damage as a discretization problem under the continuum hypothesis of the finite element method (FEM) (e.g., the eXtended Finite Element Method (XFEM) is the most successful paradigm among the generalized FE procedures for the simulation of embedded discontinuities in materials), CDM deals with the introduction of damage through a material constitutive approach. Further details about the application of CDM to laminated composite architectures are provided throughout the chapter. The computational standpoint is complemented with the description of experimental techniques and equipments commonly employed for testing composite specimens under impact events. Nondestructive inspections (NDI) of such impacted specimens constitute a valuable source of information for the interpretation of the damage mechanisms whose reproduction through numerical simulation is pursued. Besides, the chapter assesses, for different composite configurations, the correlation between ballistic experimental curves in HVI (penetrating) regime and the numerical results achieved with Abaqus/Explicit code by applying the modeling strategies discussed. Computational models presented hereafter were developed by IMDEA Materials Institute.

The competitive specific ballistic performance of composites, together with matured modeling strategies and the improved computational capabilities available nowadays suggest a promising future of composite-based vehicle shielding configurations. Moreover, the presented modeling strategies are appropriate to evaluate the impact performance of existing materials, as well as to design new solutions for impact shielding. This technological challenge is addressed in a dedicated section of this chapter, where the conception of hybrid shields and their virtual design are exposed. Emphasis is put on the worth of the progressive enhancement of the modeling strategies for the development of a robust, reliable and accurate virtual testing roadmap.

8.12.2   Computational Modeling of Impact on Composite Materials

For the approach described in this chapter, a laminate (**Fig. 1(a)**) is considered the fundamental mesomechanical unit. It is composed of a layup of plies with their local material directions arranged according to a stacking sequence referred to a global direction (**Fig. 1(c)**). The individual plies are commonly made of UD, woven or braided fibers embedded in a thermoset or thermoplastic matrix. Carbon/epoxy and glass/epoxy plies are examples of FRP, although a composite laminate can be built up, in general, from many other materials. An example are the so-called fiber metal laminates (FML), such as glass-reinforced aluminum laminates (GLARE), typically composed of aluminum sheets stacked together with UD or 2D woven glass/epoxy prepregs (**Fig. 1(d)**).

FRP laminates possess excellent stiffness and strength properties under the action of in-plane loads (**Fig. 1(a)**). However, impact loads are generally applied in the perpendicular direction to the plane of the laminate, thus producing a complex
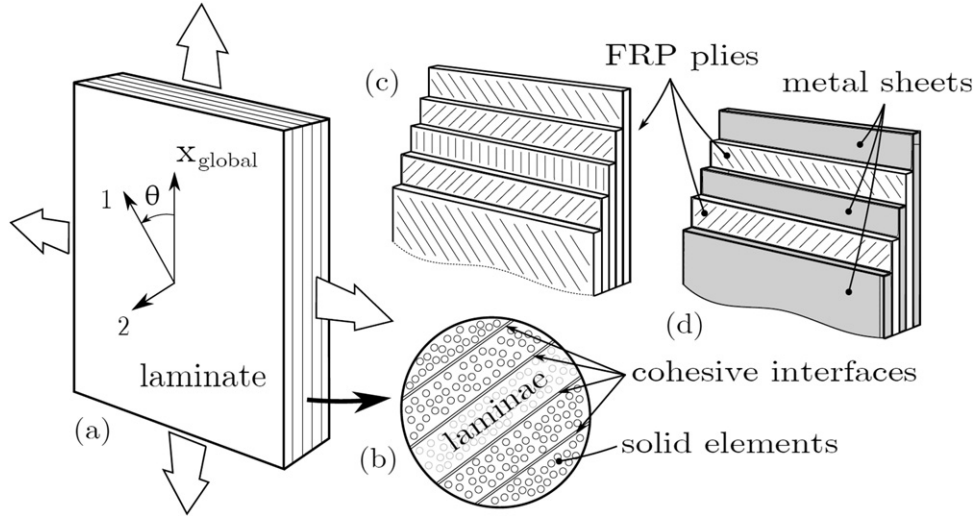
Fig. 1 (a) Schematic representation of a composite laminate subjected to global load, (b) mesomechanics discretization of individual laminae (intraply damage) and interfaces (interply damage) using solid elements and cohesive interfaces, respectively, (c) and (d) mesomechanical representation of a fiber reinforced polymer (FRP) angle ply laminate and a fiber metal laminate (FML).

three-dimensional (3D) stress field in the composite. The out-of-plane components of the stress tensor can only be captured properly if plies are modeled with solid or continuum shell elements (**Fig. 1(b)**). Moreover, this 3D discretization allows the explicit introduction of interfaces between plies. Interply delamination can be simulated by means of cohesive elements or surface interactions.

8.12.2.1 Material Models for Laminated Composite Materials

8.12.2.1.1 Isotropic damage model for metal layers

The Johnson–Cook material model has been assumed to characterize the behavior of the aluminum plies in the FML, taking into account the yield limit region (σ_y) and the strain to failure (ε_f). This is an accepted model for high strain metals, such as aluminum, which takes into account strain rate and thermal effects,[22] and is expressed as:

$$\sigma_y = (A + B \cdot \varepsilon^n) \cdot \left(1 + C \cdot Ln\dot{\tilde{\varepsilon}}\right) \cdot \left(1 - \tilde{T}^m\right) \tag{1}$$

wherein σ_y is the effective stress, ε is the effective plastic strain, $\dot{\tilde{\varepsilon}}$ is the normalized effective plastic strain rate (normalized to 1.0 s^{-1}), $\tilde{T}$ is the normalized temperature defined as follows:

$$\tilde{T} = \frac{T - T_{room}}{T_{melt} - T_{room}} \tag{2}$$

where T_{room} is the room temperature and $T_{melt} = 775$ K is the aluminum melting point. The material parameters A, B, C, n and m are respectively the static yield limit, the strain hardening modulus, the strain rate coefficient, the strain hardening exponent and the thermal softening exponent. Their values are available in the literature[23] as $A = 369$ MPa, $B = 684$ MPa, $C = 0.0083$, $n = 0.73$ and $m = 1.7$ for the 2024T4 aluminum alloy. The effective plastic strain at failure is defined as:

$$\varepsilon_f = \left(D_1 + D_2 \cdot e^{D_3 \cdot \sigma^*}\right) \cdot \left(1 + D_4 \cdot Ln\,\dot{\tilde{\varepsilon}}\right) \cdot \left(1 + D_5 \cdot \tilde{T}\right) \tag{3}$$

where ε_f is the failure strain, σ^* is the mean stress normalized by the effective stress (triaxiality), $\dot{\tilde{\varepsilon}}$ and $\tilde{T}$ were defined previously. D_1, D_2, D_3, D_4, and D_5 are material parameters which govern the damage dissipation in the material up to final failure. They are adopted from the literature[24] as $D_1 = 0.112$, $D_2 = 0$, $D_3 = -1.5$, $D_4 = 0.007$, and $D_5 = 0$. The fundamental properties of aluminum 2024 also needed in the model are shown in **Table 1**. Damage evolution has been specified through a single value of fracture energy of 9570 kJ $\cdot$ m^{-2}.

8.12.2.1.2 Orthotropic damage model for unidirectional composite plies

The constitutive model for the elements that simulate the plies is based on homogenized properties at the mesomechanical scale. In the case of FRP, linear elastic orthotropic behavior (nonlinear relationship is usually adopted in the case of shear loading) previous to the onset of damage is defined with the nine engineering constants E_1, E_2, E_3, G_{12}, G_{13}, G_{23}, v_{12}, v_{13} and v_{23}, and the strength properties associated to the different loading directions. Damage at the two discretization levels (intra and interply) is introduced as a degradation of the original undamaged stiffness. Upon damage initiation, damage is therefore defined from material standpoint as an extension of the constitutive laws. This strategy does not require the explicit introduction in the

Table 1   Fundamental material properties of aluminum 2024

Parameter	Aluminum 2024
	Value
Density, ρ (kg/m^3)	2770
Poisson ratio, (v)	0.33
Elastic modulus, $E(GPa)$	73.1
Specific heat $c_p(J/kgK)$	875
Melting temperature $T_{melt}(K)$	775

discretization of the discontinuities produced by the damage, i.e., the breakage of elements and subsequent remeshing. On the contrary, the elements degrade their constitutive response up to the point when they are effectively erased from the model, once the absorbed energy in the damage process reaches the fracture energy of the material.

The onset of damage for each failure mode is triggered at each ply (fiber breakage/kinking, matrix cracking, etc.) and cohesive interface (interlaminar tension/shear) when the local stress components and the undamaged strengths of the material verify the failure criteria selected for the implementation. As previously mentioned, different formulations are available in the literature. Once the damage is present in the material, its progression is governed by a softening effect in the corresponding stress–strain curve, dependent on the fracture energies, which can be experimentally determined.

Unidirectional fiber-reinforced composite plies are modeled by means of 3D CDM based on the work of Maimí et al.[13,25] The composite is considered to follow different elastic behavior according to orthotropic direction until the first-ply failure is detected by means of a failure surface which is obtained from computational micromechanical simulations of a representative volume element of the UD composite ply,[26–31] and that can be defined by different loading functions according physically-based 3D failure criteria developed by Catalanotti et al.[32] A nonlinear elastic-damageable behavior is considered for in-plane and out-of-plane shear responses, based on the Ramberg–Osgood law.[33] The gradual degradation of the stiffness of a ply after damage onset is simulated by means of appropriate progressive damage evolution laws according to different damage modes.[34] The ply compliance tensor, **H**, is given by

$$\mathbf{H} = \begin{bmatrix} \dfrac{1}{(1-d_1)E_1} & -\dfrac{v_{12}}{E_1} & -\dfrac{v_{13}}{E_1} & 0 & 0 & 0 \\[2ex] -\dfrac{v_{12}}{E_1} & \dfrac{1}{(1-d_2)E_2} & -\dfrac{v_{23}}{E_2} & 0 & 0 & 0 \\[2ex] -\dfrac{v_{13}}{E_1} & -\dfrac{v_{23}}{E_2} & \dfrac{1}{(1-d_3)E_3} & 0 & 0 & 0 \\[2ex] 0 & 0 & 0 & \dfrac{1}{(1-d_6)G_{12}} & 0 & 0 \\[2ex] 0 & 0 & 0 & 0 & \dfrac{1}{(1-d_5)G_{13}} & 0 \\[2ex] 0 & 0 & 0 & 0 & 0 & \dfrac{1}{(1-d_4)G_{23}} \end{bmatrix} \tag{4}$$

wherein $d_{M,\ M=1,\ldots,6}$ are scalar damage variables associated with longitudinal ($M=1$) and transverse directions ($M=2$), for in-plane loads, and d_3 for out-of-plane loads. The damage variables d_4, d_5, and d_6 affecting the shear stress components are influenced by longitudinal and transverse cracks. In the current laminate modeling approach d_3 is not activated since the overall out-of-plane stiffness degradation is addressed by the ply interface damage model.

The elastic domain is assumed to be bounded by four distinct damage activation functions associated with damage in the longitudinal ($N=1+,\ 1-$) and transverse ($N=2+,\ 2-$) directions:

$$F_N = \phi_N - r_N \leq 0 \tag{5}$$

wherein the $+$ and $-$ signs indicate tension ($+$) and compression ($-$). The loading functions, ϕ_N can be obtained by homogenization of the numerically-predicted failure behavior of the ply under multiple load combinations, represented in **Fig. 2**, and coded as three-dimensional (3D) failure criteria based on the physical description of each failure mode.[32] They take into account the apparent increase of the transverse tensile strength (Y_{is}^T) of an embedded ply according to its thickness and position in the laminate,[35] also known as the "in-situ effect."[36]

The elastic domain thresholds, r_N in Eq. (5), are obtained applying the Kuhn–Tucker and consistency conditions, and are related to the damage variables by damage evolution laws. They couple the elastic domains in tension/compression and uncouple those in transverse/longitudinal directions, and only increase from initial unit value when damage evolves. That is[25]:

$$r_{N+} = \max\left\{1, \max_{s=0,t}\left\{\phi_{N+}^s\right\}, \max_{s=0,t}\left\{\phi_{N-}^s\right\}\right\}, \quad N=1,2$$
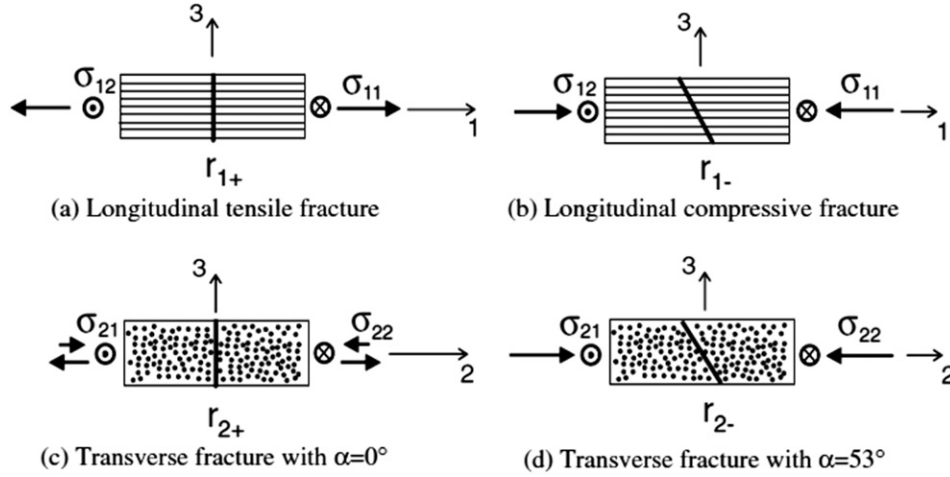
Fig. 2 Fracture surfaces and corresponding continuum damage mechanics (CDM) internal variables.
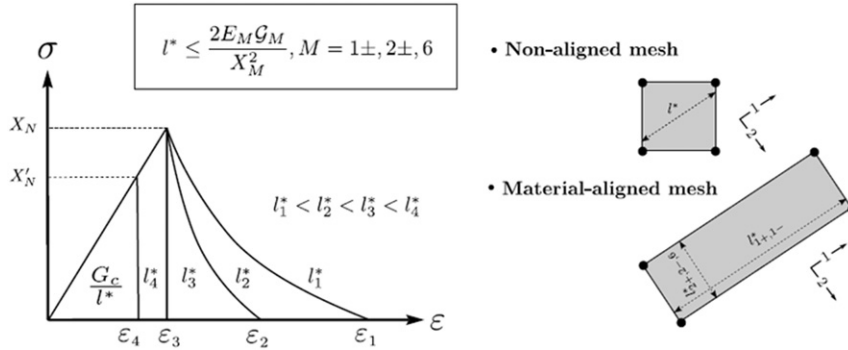
Fig. 3 Mesh regularization strategy used in the composite ply damage model.

$$r_{N-} = \max\left\{1, \max_{s=0,t}\left\{\phi_{N-}^s\right\}\right\}, \quad N = 1, 2 \tag{6}$$

Damage evolution is described by exponential softening laws expressed in the following general form:

$$d_M = 1 - \frac{1}{f_N(r_N)} \exp\{A_M[1 - f_N(r_N)]\} f(r_K) \tag{7}$$

wherein the function $f_N(r_N)$ is selected to force the softening of the constitutive relation and $f(r_K)$ is the coupling factor between damage laws and elastic threshold domains. The damage law parameters A_M ($M = 1\pm$, $2\pm$, 6) are calculated to ensure the objectivity of the strain softening solution with respect to fracture energy within a crack band of typical element length l^*, as proposed by Bažant and Oh.[17] There is a maximum element size that guarantees the correct representation of both material strength and fracture energy dissipation simultaneously:

$$l^* \leq \frac{2E_M \mathcal{G}_M}{X_M^2}, M = 1\pm, 2\pm, 6 \tag{8}$$

where E_M, G_M, and X_M are, respectively, the Young modulus, the fracture toughness and the ply strengths corresponding to each failure mode. If l^* is too large, the strength of the material associated with such an element is reduced while maintaining the respective fracture toughness constant, as illustrated in **Fig. 3**.

Another source of mesh-dependence in strain localization models is mesh-induced direction bias. Moreover, the misalignment between crack band direction and mesh lines induces stresses locking because of the continuity in displacement of the FE method.[37] Advanced numerical techniques are available to mitigate this pathological behavior for general crack paths.[38] In UD composites, microstructure dictates that matrix cracks develop parallel to fiber direction while fiber breakage and kinking tend to occur transverse to it. Therefore, an engineering solution to mesh-induced bias in such materials is the alignment of mesh lines with orthotropic material directions, as proposed in Lopes et al.[39]

In arbitrarily-aligned meshes, l^* represents a typical cracking distance across the surface of an element, and the effective thickness of the softening band depends on the orientation of the crack with respect to the mesh lines. For a squared-surface element mesh, the thickness of a zig–zag band in the diagonal direction is $\sqrt{2}$ times larger than if the band propagates parallel to the element sides.[37] For material-aligned meshes in UD composites, two independent characteristic lengths, $l^*_{1+,1-}$ and $l^*_{2+,2-,6}$ can be devised, respectively for fiber and matrix crack banding, that correspond exactly with element surface sides, hence allowing rectangular elements and mesh coarsening. A maximum element aspect ratio of 3:1 ($l^*_{1+,1-} \leq 3 \times l^*_{2+,2-,6}$) guarantees the correct representation of both material strength and fracture toughness for all damage modes and avoid large element aspect ratios which would introduce numerical difficulties.

Another advantage of using material-aligned meshes is that it facilitates the use of element erosion to simulate cracks in the material in the strong sense. i.e., with kinematic discontinuities between crack faces. The disadvantages are that the material that would otherwise be stress resistant is removed and that crack faces are generated at a relative distance between each other, corresponding to the thickness of the crack-band. The first effect is mitigated by the fact that stresses around a crack need a finite distance to recover to nominal values, according to a shear-lag assumption. The second consequence of crack-band erosion would only have effect on compressive and shear dominated cracking. Hence, in this work element erosion is only used in tensile failure modes. FEs are eroded when the damage variables d_{1+} or d_{2+} reach a value close to unity. The material properties required by the continuum damage model to simulate the behavior of the AS4/8552 plies are given in **Table 2**.

8.12.2.1.3 *Interlaminar mixed-mode cohesive-frictional behavior*

The ply interlaminar response is modeled by means of a classical cohesive zone method coupled with frictional behavior. The constitutive equation that couples both phenomena relates the displacement jump across the interface (Δ) to the traction vector acting on it (τ) by means of a single normalized scalar damage variable (d) to simulate delamination and friction under the full range of modes (mode II or sliding mode-τ_1; mode III or tearing mode-τ_2; mode I or opening mode-τ_3) and mode mixities:

$$\tau = \begin{Bmatrix} \tau_1 \\ \tau_2 \\ \tau_3 \end{Bmatrix} = (1-d)K \begin{Bmatrix} \Delta_1 \\ \Delta_2 \\ \Delta_3 \end{Bmatrix} - dK \begin{Bmatrix} 0 \\ 0 \\ \langle -\Delta_3 \rangle \end{Bmatrix} + \mu dK \begin{Bmatrix} \langle -\Delta_3 \rangle \dfrac{\Delta_1}{\Delta_s} \\ \langle -\Delta_3 \rangle \dfrac{\Delta_2}{\Delta_s} \\ 0 \end{Bmatrix} \tag{9}$$

wherein $\Delta_s = \sqrt{\Delta_1^2 + \Delta_2^2}$ and K is a scalar penalty contact stiffness that describes the linear-elastic behavior of the interface prior to damage initiation, and under any compressive normal tractions which are assumed not to cause damage to the interface ($\langle X \rangle = \max(0, X)$). Coulomb-type friction is introduced by the coefficient μ. The penalty stiffness is a nonphysical numerical parameter that should be large enough to ensure displacement continuity in the absence of interface damage while avoiding convergence difficulties due to ill-conditioned stiffness matrix.

This coupled cohesive-friction approach is implemented in the kinematics of surface contact interactions and is available in Abaqus/Explicit.[40] It is used in this work to include the significant effect of friction occurring during and after ply delamination. The shear stresses caused by friction at the interface are ramped progressively and proportional to the degradation of the interface, thus once the interface is fully delaminated, the surface interaction is uniquely governed by a dry friction model, $\tau_{1,2} = \mu K \langle -\Delta_3 \rangle (\Delta_{1,2}/\Delta_s)$. Furthermore, friction also affects the cohesive response as shear stresses are ramped with the interface damage variable, as schematically illustrated in **Fig. 4**. This causes an increase of the interface shear resistance that is function of the normal compressive tractions applied on it. The combined effect of friction and cohesive behavior has been addressed by other authors,[41] whose works eventually led to the development of cohesive element formulations that take both mechanisms into account; a capability similar to the one used in this work with cohesive–frictional surface interactions.

For the pure cohesive response, damage onset is controlled by a quadratic interaction criterion that is a function of the interlaminar strength values for each of the damage modes (τ_i°):

$$\left(\frac{\langle \tau_3 \rangle}{\tau_3^\circ} \right)^2 + \left(\frac{\tau_2}{\tau_2^\circ} \right)^2 + \left(\frac{\tau_1}{\tau_1^\circ} \right)^2 = 1 \tag{10}$$

Table 2 Fundamental material properties of AS4/8552

Parameter	AS4/8552 Value
Density, ρ (kg/m^3)	1790
Elastic modulus E_1, E_2, E_3 (GPa)	137.8, 8.6, 8.6
Shear modulus G_{12}, G_{13}, G_{23} (GPa)	4.9, 4.9, 2.8
Poisson ratio ν_{12}, ν_{13}, ν_{23}	0.35, 0.48, 0.48
Fiber direction ply strength X^T, X^C (MPa)	2042, 1495
Fiber perpendicular ply strength Y^T, Y^C (MPa)	66.1, 257
In-plane shear strength S^L (MPa)	105.2
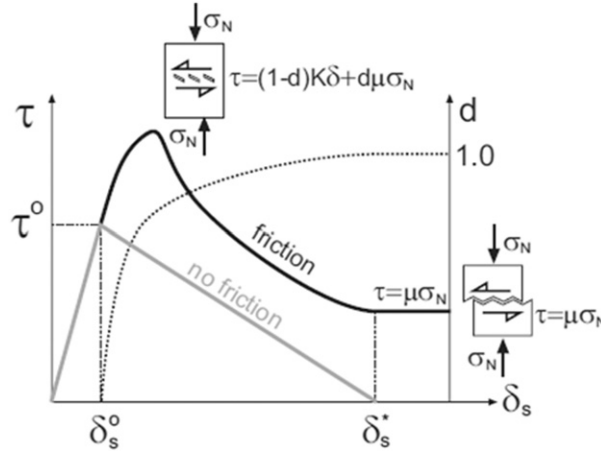
Fig. 4 Schematics of the shear response of the damage-friction model for fiber/matrix interfaces.

wherein only positive normal tractions affect the criterion. Once delamination is initiated, the cohesive tractions transferred through the interface decrease linearly to zero according to the energy-based Benzeggagh–Kenane (BK) damage propagation criterion,[42] that accounts for the dependence of the fracture energy dissipation on the mixity mode:

$$G_c = G_{Ic} + (G_{IIc} - G_{Ic})\left(\frac{G_{\text{shear}}}{G_I + G_{\text{shear}}}\right)^{\eta} \tag{11}$$

where G_{Ic} and G_{IIc} are the critical energy release rates for delamination in mode I and mode II, respectively, and $G_{\text{shear}} = G_{II} + G_{III}$.

Interlaminar fracture characterization experiments conducted by the authors, as well as results available in the literature,[43] indicate that the critical energy release rates for modes I and II are dependent on the angle between fiber directions of interfacing plies (interface angle). For $0°/0°$ interfaces in AS4/8552 laminates $G_{Ic} \approx 300 \ \text{J} \cdot \text{m}^{-2}$ and $G_{IIc} \approx 800 \ \text{J} \cdot \text{m}^{-2}$, whilst for $+45°/-45°$ interfaces $G_{Ic} \approx 600 \ \text{J} \cdot \text{m}^{-2}$ and $G_{IIc} \approx 1600 \ \text{J} \cdot \text{m}^{-2}$. Furthermore, the variation of these parameters with interface angle seems to be rather linear. Therefore, linear interpolation rules between these values are used in this work to define G_{Ic} and G_{IIc} values for different interfaces. The exponent $\eta = 1.5$ was found by least-square fit of the fracture toughness values under different mixed-mode ratios on $0°/0°$ interfaces. The opening mode interface strength is assumed equal to the ply transverse tensile strength (($\tau_3° = Y^T$) whilst the one corresponding to the shear modes was characterized by means of the short beam interlaminar shear strength (ILSS) test ($\tau_1° = \tau_2° = \text{ILSS} = 109$ MPa).

A few authors have studied the subject of friction between composite laminates including friction between delaminated surfaces.[44] Similarly to the fracture toughness parameters, the friction coefficient appears to be a function of the interface angle. For $0°/0°$ interfaces it can be as low as $\mu = 0.25$ whilst for $0°/90°$ interfaces it can be as high as $\mu = 0.75$. Hence, a linear interpolation rule between these values was used in this work to define the interface friction coefficient for different interfaces.

8.12.3 Impact Testing Experimental Techniques

Impact tests on composite materials are usually classified between LVI and HVI. An example of the first group could be the falling tool during maintenance operations, whereas the impacts of runaway debris or fragments from an uncontained engine rotor failure are examples of the second one. Godwin and Davies[45] proposed a criterion to distinguish a given impact between the two aforementioned categories; they defined a ratio between the impact velocity (V_i) and the speed of sound of the composite laminate in the through-thickness direction (c_z). If this ratio is greater than the failure deformation in the through-thickness, the impact is classified as HVI; if it is smaller, the impact corresponds to a LVI impact. In practice, LVI impacts mean masses of the order of kilograms, impacting at velocities up to $10 \ \text{m} \cdot \text{s}^{-1}$. By the other hand authors that study HVI impacts usually use masses up to 100 g impacting at velocities from $50 \ \text{m} \cdot \text{s}^{-1}$. Experimental tests of LVI impacts are performed using drop weight tower, whereas HVI impacts use gas guns.

The use of gas guns to perform HVI impact tests was popularized in the 1980s. Previously, gun powder guns had been used, but the difficulty in controlling the impact velocity motivated the use of guns that impel the projectile with gas. In addition, the use of projectiles with different geometries is limited using powder guns. Gas guns can be of one or multiple stages. This work is focused on the single stage type, since the others are used for hypervelocity (in which the velocities are measured in kilometers per second).

The operation of a gas gun is described next. It uses a vessel in which the gas is stored that is connected to a barrel with a valve. The projectile to be launched is placed at the beginning of the barrel and when the valve opens, the gas stored is released through the barrel accelerating the projectile. The key point of this experimental equipment is the valve that has to be very fast in the

opening process, leaving a clear pass of the gas. The velocity of the projectile is easily controlled by the pressure of the vessel, and the projectile could be any that fits inside the barrel.

Usually the gas guns utilize air or helium to impel the projectile depending on the range of velocity desired. In the single stage gas guns, the velocity limit is imposed by the fluid speed of sound, which is (at 0°C and at 1 atm of pressure) 331 m·s^{-1} for the air and 965 m·s^{-1} for the helium; hydrogen has an even higher speed of sound (1225 m·s^{-1}), but its use is limited because of its combustion capacity. Gas guns that are designed to use helium usually use small vessels (the volume is of the order of litres) at high pressures (around 300 bars). On the other hand, the launchers that are designed to use compressed air (cheaper) have larger vessels (volumes of the order of a cubic meter) with smaller pressures (around 10–20 bars). Another way to increase the impact velocity is to connect the barrel end with a vacuum chamber in which the specimen to impact is placed. The absence of air diminishes the resistance and increases the launcher efficiency; using such facility it is possible to impel with hydrogen, because the absence of air limits the possibility of combustion.

It has been previously stated that one of the main advantages of gas guns compared to powder guns is the possibility of launching any projectile. Associated to this versatility there is an important drawback, that is the need of a sabot to hold the projectile during the acceleration, in the case that the projectile has not the exact dimensions of the barrel (which in practice never happens). The materials used to manufacture the sabot need to be light in order to not to diminish the impact velocity of the projectile, they also have to be soft in order to not to damage the barrel interior, and finally strong enough to withstand an extreme acceleration (e.g., the maximum acceleration for an impact velocity of 800 m·s^{-1} in a 4 m long barrel is $2 \cdot 10^5$ m·s^{-2}). Since the barrel is commonly made of steel, the materials of the sabots use to be aluminum (to resist the acceleration) and foam or a polymer in order to not to increase its weight. Regarding the sabot geometry, it has to be designed in order to separate from the projectile once it is out of the barrel (by means of aerodynamic forces) in order to not to impact against the specimen.

When using a gas gun, it is necessary to have a device to measure the impact velocity. A laser barrier is probably the most common solution since it is cheap, works with any type of material, and has a good precision. Another way to measure the impact velocity is a high speed camera that films the projectile trajectory, and with the appropriate scale, can be used to measure the distance traveled in a given time. This last method is much more expensive but also more accurate. The measurement of the residual velocity in case of specimen penetration could not be performed with a laser barrier, because it does not distinguish between projectile and other fragments, and hence a high speed camera should be used. The use of high speed cameras is also very useful in order to visualize the impact process. The best combination is to place at least a front camera to film the impact face and a rear camera to film the back face movement.

The experimental tests that are shown in this work were performed using a single stage gas gun, which uses air to impel the projectile; it has a 1.5 m^3 vessel and the maximum pressure that could withstand is 6 bars. The barrel diameter is 60 mm and its length 18 m (Fig. 5). A laser barrier in the barrel mouth gives information of the impact velocity. Two high-speed cameras Photron SA-Z were used, one pointing the front face and the other one pointing the back face. Both of them were placed with a 45 degree angle with respect to the projectile trajectory in order to measure both the impact and the residual velocity.

### 8.12.3.1   Impact Tests on Monolithic AS4/8552 Panels

The objective of the tests performed was to analyze the behavior of AS4/8552 composite flat panels subjected to a spherical steel projectile impact of 20 and 30 mm in diameter. Plies of nominal thickness 0.184 mm were stacked following a layup sequence of $[45/90/-45/0]_{2s}$ yielding a total laminate thickness of 2.94 mm. The specimen size was 280×280 mm^2; a steel frame was used to hold the specimen, clamping over 15 mm at each boundary, resulting in a free span area of 250×250 mm^2 as impact zone, that is approximately 10 times the characteristic diameter of the projectile. In order to determine the ballistic limit for the two different impactor geometries, impact tests were performed at different impact velocities, ranging from non-penetration tests to total perforation. As explained before, tests were recorded by means of two high speed cameras focused to the impact and back faces,

Fig. 5   Gas gun general view at University Carlos III of Madrid facilities.
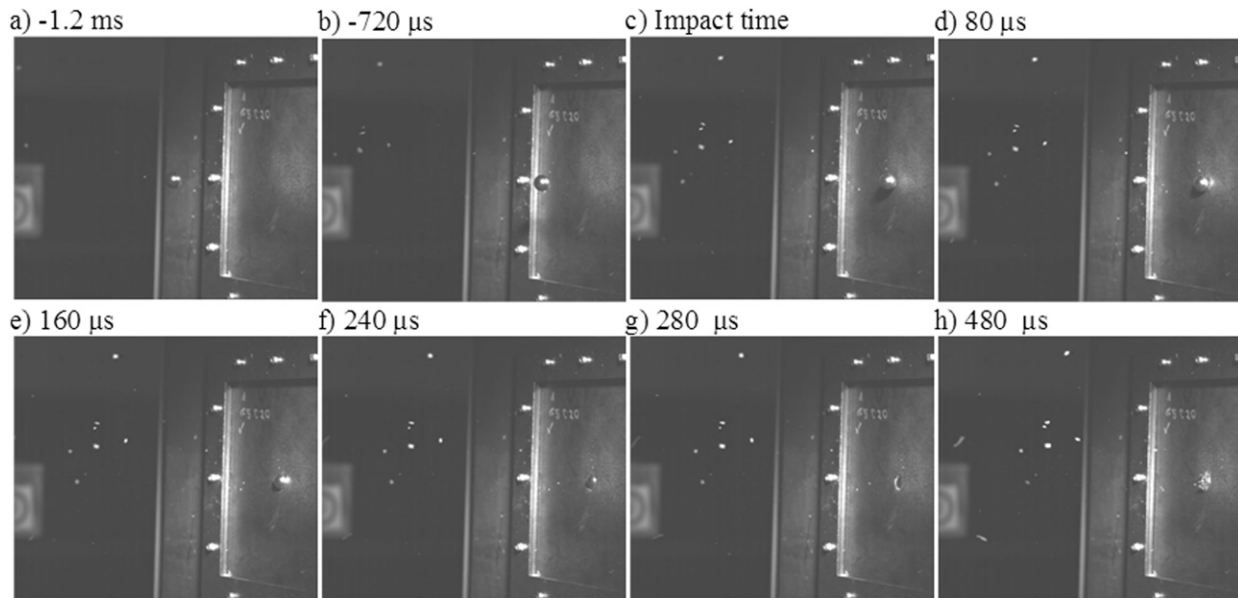
**Fig. 6**   AS4/8552 panel and 20 mm projectile. Impact face sequence.
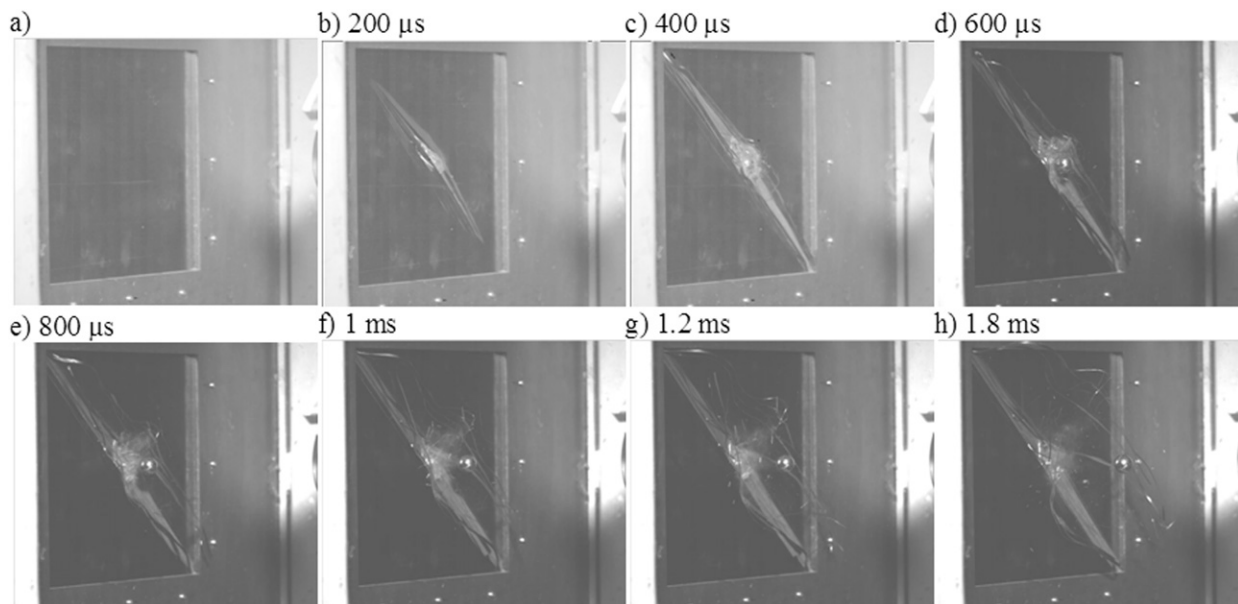
Fig. 7   AS4/8552 panel and 20 mm projectile. Back face sequence.

respectively. For instance, the sequence of the impact of a 20 mm projectile against an AS4/8552 panel is shown in **Figs. 6** and **7** (front and back face, respectively).

The image treatment allows to track the displacement of the projectile and therefore, to calculate the impact projectile velocity (V_i) and the residual projectile velocity (V_R) in case of perforation. In the following figures, the experimental residual velocity obtained was plotted versus the impact velocity for each case. Also, these data were fitted by least-square regression according to the Lambert–Jonas equation (1976):

$$V_R^P = A\left(V_i^P - V_{50}^P\right) \tag{12}$$

where A and P are regression coefficients, and V_{50} is the ballistic limit velocity (defined as the velocity of the projectile to perforate the target 50% of the times). **Fig. 8** exhibits, for the two different projectile diameters, 20 and 30 mm, the evolution of the residual velocity with the initial impact one. The intersection of the Lambert–Jonas curve with the impact velocity axis leads to the ballistic limit estimation being $V_{50} = 69 \ \text{m} \cdot \text{s}^{-1}$ and $V_{50} = 55 \ \text{m} \cdot \text{s}^{-1}$ for 20 and 30 mm spherical projectile diameters, respectively.
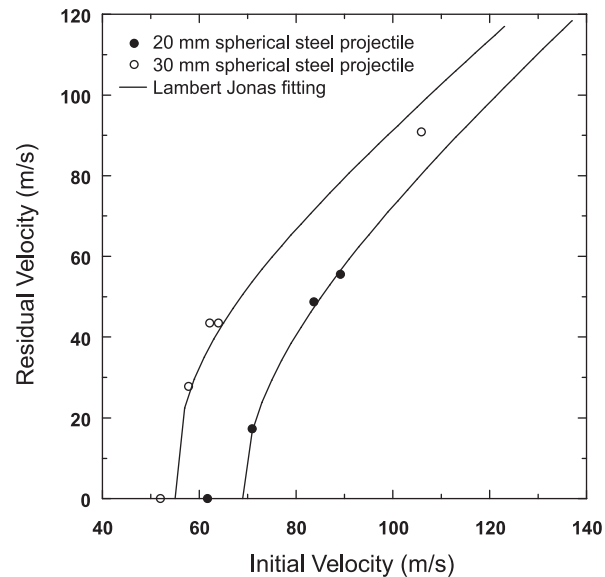
Fig. 8 Ballistic curves of the AS4/8552 panels subjected to impact with 20 and 30 mm diameter spherical projectiles.

When increasing the projectile diameter there are two opposite effects. By one side the mass is higher and hence the penetration capacity increases; by the other, the front area is larger and hence more laminate area responses against the penetration, reducing the penetration capacity. Finally the first effect dominates since it increases with the cubic of the diameter and the second one with the square.[46]

8.12.3.2   Impact Tests on GLARE Panels

The coupons were experimentally tested by Yaghoubi and Liaw,[47] who also performed a detailed discussion of numerical results obtained with LS-DYNA software, including comparisons of ballistic curves and failure mechanisms. Beams of 254 mm span and 25.4 mm width with different layup sequences of 2024-T3 aluminum sheets (0.305 mm thickness) and UD S2-glass/epoxy prepregs (0.127 mm thickness) stacked in 0 and 90° directions were studied. An erodible, bullet-shaped copper projectile was shot with a high-speed gas gun at velocities above $100 \text{ m} \cdot \text{s}^{-1}$ against the GLARE targets. A fixity system to clamp both ends of the beam coupons over a length of 50.8 mm was employed, resulting in a free span length of 152.4 mm, which was the length of beam represented in the FEM simulations, clamped at its ends.

A high-speed camera was situated perpendicular to the bullet trajectory to measure its velocity. The beam specimens were equipped with strain gauges at the impact face in order to monitor the transient dynamic strain histories at gauges locations and compare them to FE predictions. A complete postimpact damage assessment was performed, including optical imaging and destructive evaluation. The impacted targets were split to uncover their cross-sections at the impact zone. The damage patters observed in the experiments were compared to the numerical results. Typical damages of fiber-reinforced polymer matrix composites (e.g., matrix cracking, fiber breakage, and delamination) were observed. In addition, failure mechanisms induced by the presence of metal layers were identified, in particular, plastic hinging, petalling, and plugging. This rich damage diversity was also found with the Abaqus/Explicit simulations presented in the current chapter, see Fig. 17(b) and (c).

The experimental characterization of the impact events on GLARE was completed in Yaghoubi and Liaw[47] with the fitting of data in residual velocity versus impact velocity plots. Lambert–Jonas Eq. (12) with several exponents P were tried, resulting in barely distinguishable curves in the limit $V_R \rightarrow V_i$, while the curves mismatch in the limit $V_R \rightarrow 0$ resulted in slight deviations in the V_{50} estimations. The analysis of up to five different specimen arrangements allowed the determination of the ballistic limit V_{50} as a function of the thickness of GLARE.

8.12.4   Virtual Impact Testing of Composite Laminates

8.12.4.1   Unidirectional Carbon Fiber Reinforced Panel

8.12.4.1.1   Model description

The $[45/90/-45/0]_{2s}$ AS4/8552 composite specimens were discretized using a dual mesh approach, as depicted in Fig. 9(a), in order to minimize the computational effort: a coarse mesh of 8-node hexahedron continuum shell elements SC8R with full laminate description was selected for the damage-free outer region, while a refined mesh of 8-node, reduced integration, linear brick solid elements C3D8R was employed for the central impact zone. An enhanced-strain hourglassing control in the C3D8R
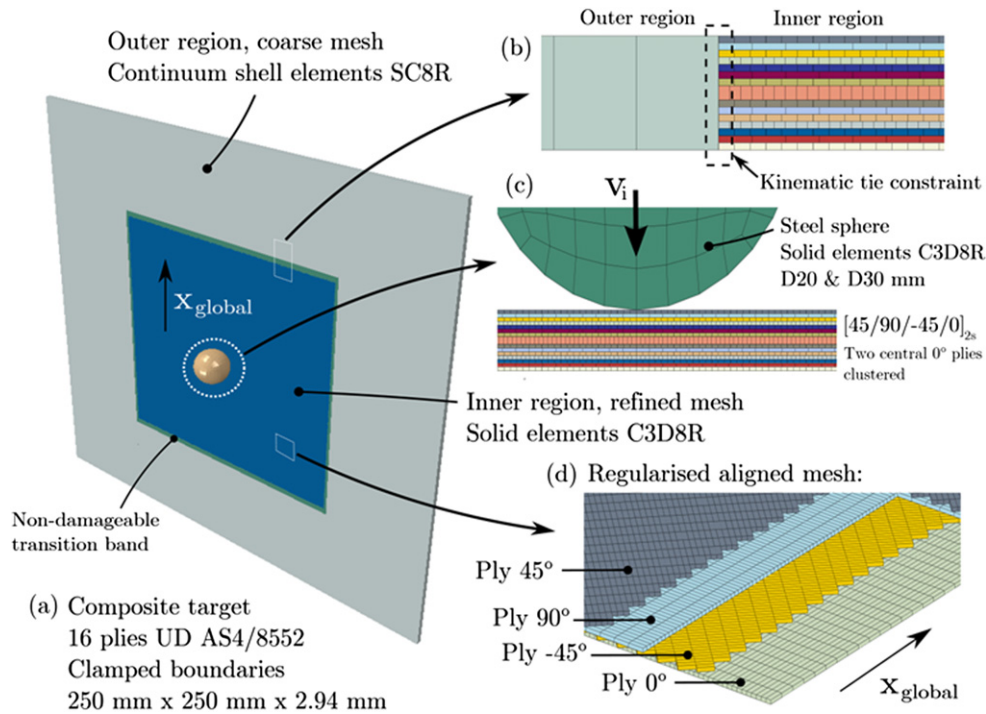
Fig. 9 Simulation strategy for the impact simulation on AS4/8552 panels: (a) global model, (b) detail of the transition region, (c) detail of the impact zone, (d) detail of the finite element discretization across plies.

elements was prescribed. One solid element per layer in the through-the-thickness direction allowed capturing properly the damage mechanisms in the impact region. Both inner and outer regions were kinematically linked by means of tie constraints relations (**Fig. 9(b)**), and a non-damageable transition band was retained at the inner–outer interfaces to prevent composite damage nucleation induced by the stress concentrations at tie constraints.

In the refined area of interest, a mesh regularization strategy with mesh lines aligned with the intrinsic fiber direction in each layer – in order to ease predominant matrix fracture cracks extension in parallel direction to fiber – was applied, leading to nonconforming meshes at the interfaces between layers (**Fig. 9(d)**). A cohesive zone model (CZM) approach was established between these nonconforming meshes with cohesive surfaces technology available in Abaqus, using contact surface pairs algorithm to reduce the computational cost of the model. The in-plane regularization of fiber- and matrix-dominated damage modes was combined with the minimum allowable crack density determined by cohesive length considerations at the cohesive interfaces, leading to critical element characteristic dimensions of $l_{ch}(1+, 1-) = 0.81$ mm and $l_{ch}(2+, 2-, 6) = 0.27$ mm.

Intraply CDM approach was incorporated to the Abaqus/Explicit model – for the elements of the central impact region – by means of a user-defined material (VUMAT) Fortran subroutine containing an evolved 3D damage version of the LaRC04 failure criteria, additionally taking into account in-situ ply strength properties computations. Abaqus element distortion control, eroded element deletion and a maximum degradation value of 0.995 were activated. Interply cohesive interactions were governed by a quadratic stress initiation criterion, and an energy-type damage evolution law with a mixed-mode Benzeggagh-–Kenane criterion was selected. Besides, the tangential behavior of the interply interactions was prescribed by a friction coefficient $\mu = 0.5$. Further friction contact interactions to avoid interpenetration of exposed internal element faces of damaged parts were included.

A plastic, rate dependent Johnson–Cook material model was defined for the steel sphere, also discretized using solid elements C3D8R (**Fig. 9(c)**). From computational simulations, however, it was observed no permanent plastic strain in the projectiles. A predefined velocity field $\mathbf{V}_i$ was specified for the set of elements that composed the impactor. The interaction impactor-laminate was defined through a hard contact pressure–overclosure relationship and a metal-laminate friction coefficient $\mu = 0.3$. A semi-automatic variable mass scaling with default target increment $\Delta t = 10^{-8}$ s was applied to the elements of the central damageable region.

8.12.4.1.2   Results

Experimental and numerical ballistic curves are shown in **Fig. 10** for the two sphere diameters tested, 20 and 30 mm. Different numerical results corresponding to different values of the parameter ε_{22d} in the range 0–10% are reported. The parameter ε_{22d} was employed in the VUMAT subroutine as the minimum strain required in matrix direction 2 to allow setting the element status variable equal to 0 once the damage variable d_{2+} has reached its maximum $d_{2+} = 1$. This is, ε_{22d} acts as an additional strain-based
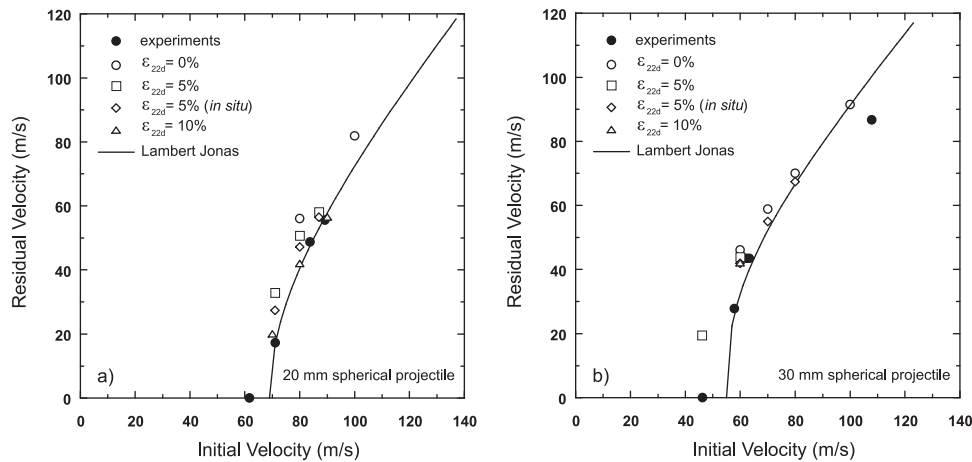
Fig. 10 Comparison of the numerical predictions of the ballistic curve of the AS4/8552 composite panels with the experimental tests: (a) spherical projectile of 20 mm in diameter, (b) spherical projectile of 30 mm in diameter.

element deletion criterion that may collect damage and strain rate effects not incorporated into the current version of the VUMAT subroutine. An additional test was performed considering the interface strength in tension τ_3° locally variable and equal to the minimum in-situ tensile ply strength in matrix direction Y^T of the two layers that share each interface. **Fig. 10** reflects the sensitivity of the analysis to changes of the mentioned parameters. In most cases, very good correlation between experimental and numerical results is observed in a wide range of impact velocities. Optimum results are found for $\varepsilon_{22d} = 5\%$ with in-situ interface strength τ_3°. Thus, satisfactory results in terms of energy dissipated in the ballistic impacts were retrieved for different projectile sizes and velocities.

Post-impact inspection of the specimens was also carried out to identify the damage mechanisms arisen in the experiments and compare them to the damage patterns retrieved from the models. **Fig. 11(a)** gathers four snapshots of the sequence of impact of a 20 mm diameter sphere against an AS4/8552 laminate. Initial contact (1) was followed by projectile indentation (2), which involved crushing of the composite material in the layers located closer to the impact face, through-the-thickness shear damage, in-plane fiber breakage and high delamination at the rear face. Hybrid local (plugging) and global (membrane-like) deformation field was observed. Step (3) corresponds to an advanced state of penetration with fast propagation of decohesion and matrix cracking following the preferential mesh lines defined with the regularization. Finally, the sphere fully pierced the laminate with a residual velocity, while the absorbed momentum contributed to the generalized delamination and fiber breakage of the rear plies of the laminate.

A detailed visual inspection of the impact face (**Fig. 11(b)**) revealed that the damage pattern of matrix cracks propagating in the local fiber direction of the external layer (45°) was effectively captured by the FEM. Localized material crushing and fiber failure at the impact footprint were also present. From the examination of the back face (**Fig. 11(c)**), a dominant damage direction was identified. This direction is determined to a great extent by the governing flexural stiffness of the laminate, which is dictated by the UD fiber orientation of the rear ply (45°). Both, coupled delamination and matrix cracking of the rear layers, evolved following the preferential (mesh alignment) direction. Besides, perpendicular cracks involving fiber breakage emanated from the impact area and propagated at $-45°$ approximately. These features were also captured with the fidelity of the model. The well-known coupling between intraply and interply damages in these architectures[48] was reproduced at most of the through-the-thickness interactions defined for building the model. **Fig. 12** illustrates the damage variable d_2 in all the plies of the laminate – numbered from impact to back face; note that the two central 0° plies of the laminate were clustered in the model into the single ply number 8 – at the refined mesh region after fully perforation of the laminate. Simulation provided d_2 bands oriented according to the preferential matrix crack direction in each ply. Layers closer to the impact face presented concentrated element deletion due to plugging and crushing mechanisms, while larger areas of d_2-damaged elements (also affected by cohesive damage) were found in the rear layers.

The superposition of all the cohesive damage regions in the different plies resulted in the delamination contours shown in **Fig. 13** (right). It was observed how intraply damage triggered decohesion of the adjacent plies. Thus, the extension of delamination areas depended strongly on the presence of cracks in matrix and fiber breakage. Left image of **Fig. 13** reports the delamination footprint obtained via C-Scan in an impacted specimen with a 20 mm diameter sphere. The inspection returned a stretched central area of full delamination oriented in the fiber direction of the back face layer (45°), thus confirming visual inspection. Two narrow bands of delamination of the rear face ply were observed, although their contribution to the global energy absorption of the composite panel was estimated small, since no fiber breakage was involved in these bands. The pursued failure mechanisms reproduction fidelity of the model is assessed in the right image of **Fig. 13**, where the FEM delamination contours are superposed on the C-Scan image. It is observed that the model captured quite approximately the size and shape of the central fully delaminated area. The two aforementioned narrow bands of delamination of the rear ply were not reproduced in the numerical
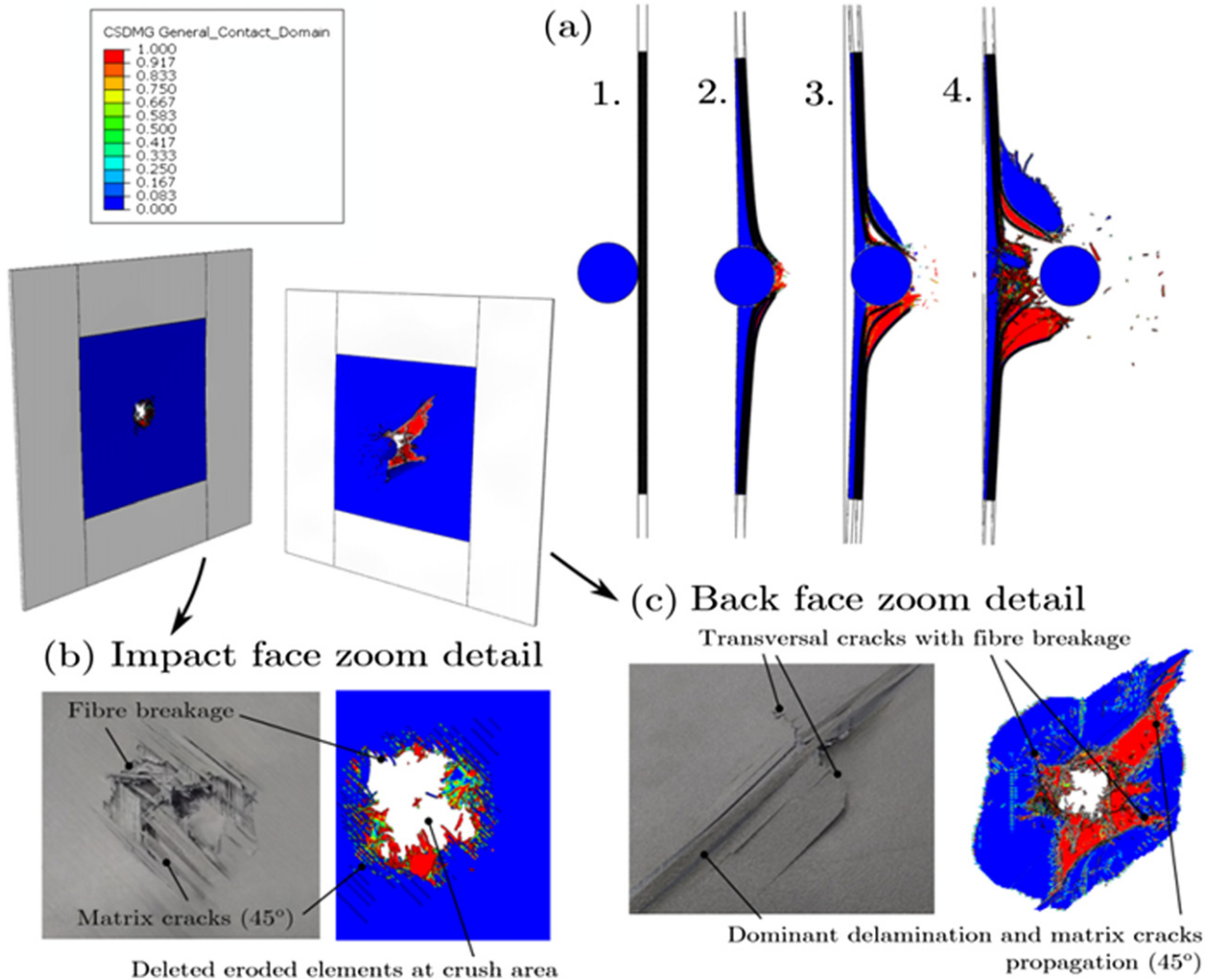
Fig. 11 Damage patterns in AS4/8552 composite panels impacted with spherical projectile: (a) impact sequence, (b) detail of the impact face of the laminate at the penetration area (experiment and simulation), (c) detail of the back face of the laminate at the penetration area (experiment and simulation).

simulation. Further refinement of the VUMAT damage subroutine and sensitivity analyses of the model discretization may help to improve the modeling strategies and push the state-of-the-art toward the horizon of high-fidelity virtual testing.

8.12.4.2   Fiber-Metal Laminated Panel

8.12.4.2.1   Model description

The discretization strategy (**Fig. 14(a)**) was similar to the one employed for the AS4/8552 benchmark case: 8-node hexahedron continuum shell elements SC8R were used for damage-free regions close to the clamped ends, and 8-node, reduced integration, linear brick solid elements C3D8R with enhanced-strain hourglassing method in the central region of interest. Due to the dissimilar thickness of the S2-glass/epoxy and aluminum plies and, of course, to the different constitutive and dynamic responses of both materials, the discretization strategy in the through-the-thickness direction was reconsidered (**Fig. 14(c)** and **(d)**). Thus, one solid element per ply was kept in the fiberglass material, while the aluminum sheets were meshed with two solid elements per sheet, in order to enhance the capture of the plastic behavior induced by the dynamic flexural loading of the laminate without penalizing the computational cost associated to finer meshes. The kinematic continuity of the outer and inner meshes was preserved by means of tie constraints relations (**Fig. 14(b)**).

   The mesh regularization in the refined area of impact was also revisited. In the fiberglass plies, mesh lines were aligned with the intrinsic UD fiber direction, yielding elements with critical characteristic dimensions $l_{ch}(1+, 1-)=0.605$ mm and $l_{ch}(2+, 2-, 6)=0.198$ mm after the conjunction of the intraply and cohesive mesh limitations. Isotropy – this is, no preferential crack propagation directions in material a priori – was induced in the aluminum layers by designing meshes of square elements of characteristic dimension (side) equal to $l_{ch}(2+, 2-, 6)$. Interactions between the resulting nonconforming meshes at the
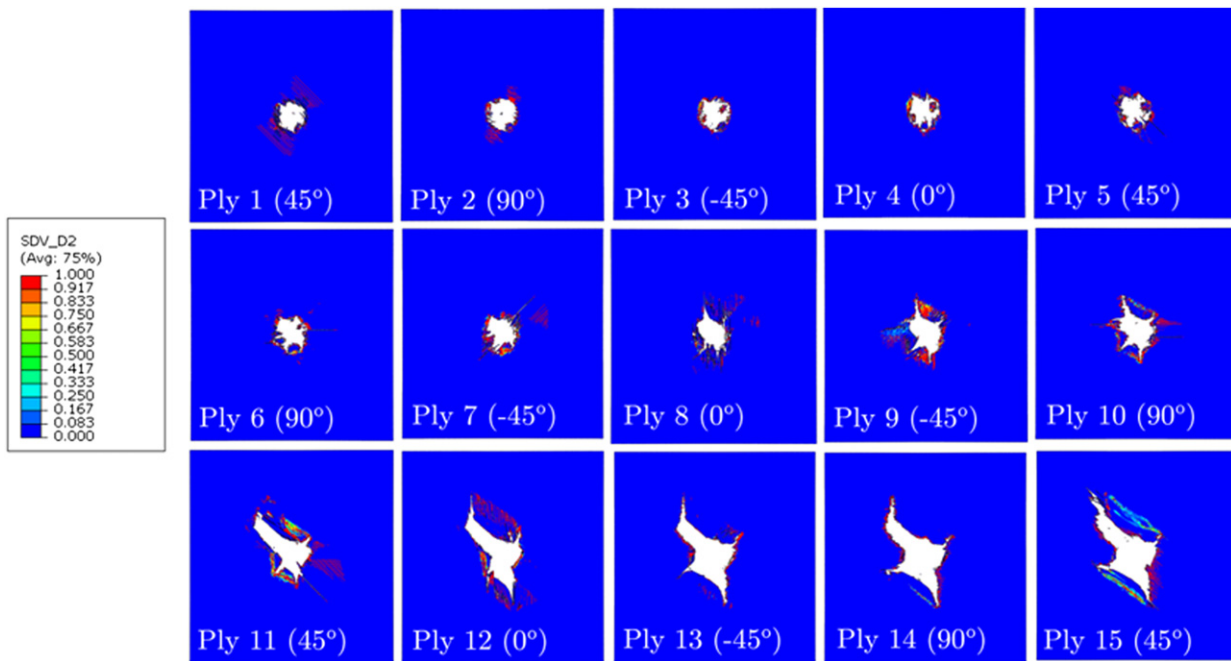
Fig. 12 Damage variable d_2 in the different plies of the $[45/90/-45/0]_{2s}$ AS4/8552 composite laminate (two central plies clustered as depicted in **Fig. 9(c)**).
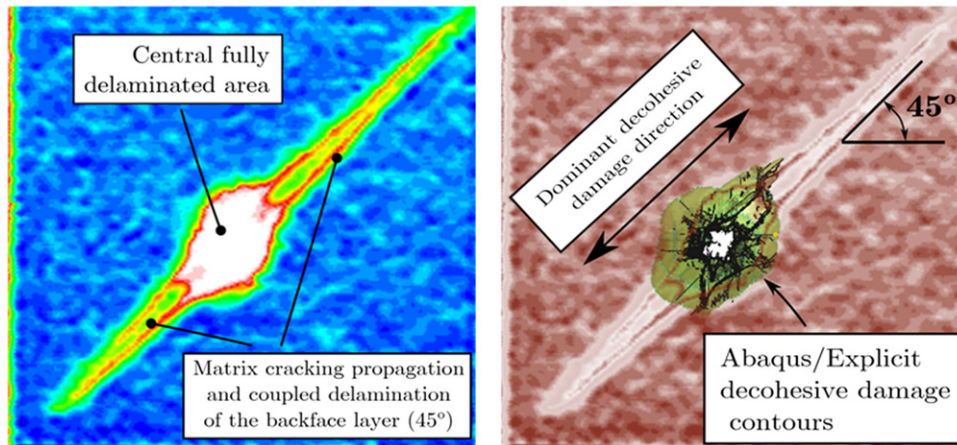

Fig. 13 C-scan inspection of one of the AS4/8552 panels impacted with a spherical projectile of 20 mm diameter and impact energy of 81 J.

interfaces between layers (**Fig. 14(d)**) were handled with cohesive surfaces technology. Due to dissimilar strengths of metal and fiberglass (dissimilar element deletion thresholds derived from the particular failure criteria used for each material), the contact algorithm included additional surface pairs to avoid potential interpenetration of nonadjacent layers in case the elements between them were eroded during the impact simulation.

For the elements of the fiberglass layers, a CDM 3D VUMAT Fortran subroutine based on LaRC04 failure criteria and in-situ ply strength properties were used. The damage criterion in the elements of the aluminum sheets was defined with the coefficients provided by Yaghoubi and Liaw[47] for the plastic, rate dependent Johnson–Cook material model. The damageable parts of the FML were prescribed with element distortion control, active eroded element deletion and maximum degradation parameter equal to 0.999. As in the AS4/8552 simulation, a quadratic stress initiation criterion and an energy-type damage evolution law with a mixed-mode Benzeggagh–Kenane criterion were used for the interply cohesive interactions. At first approach, all the interfaces, including metal–fiberglass ones, were given the strength properties of fiberglass material, in particular $\tau_3^\circ = Y_{S2-glass/epoxy}^T$ and $\tau_1^\circ = \tau_2^\circ = \tau_{13\ S2-glass/epoxy}$. A global friction coefficient $\mu=0.5$ was assumed. The copper projectile was meshed with solid elements C3D8R (**Fig. 14(c)**) and, for its constitutive and damage behavior, a Johnson–Cook material model
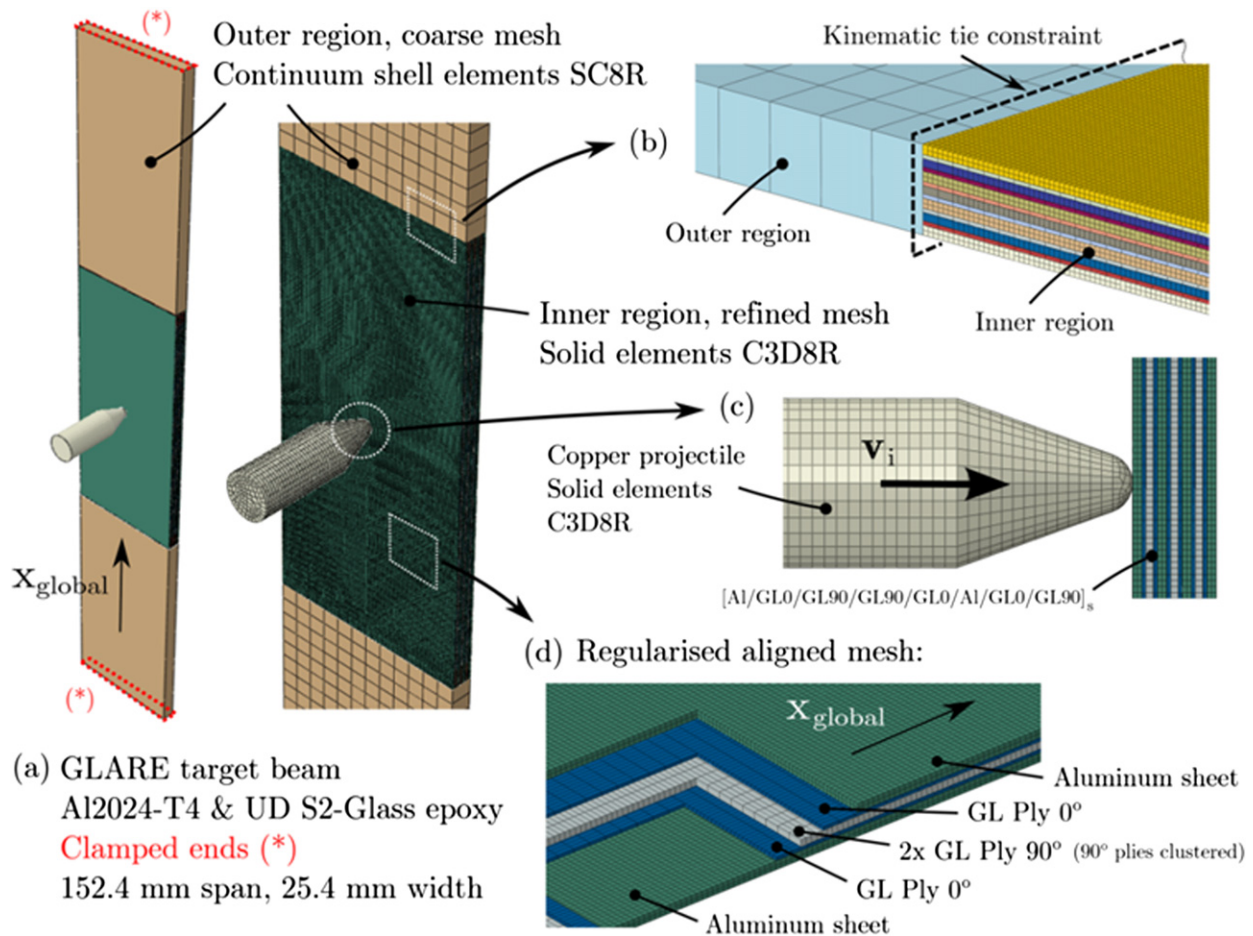
Fig. 14 Simulation strategy for the impact simulation on GLARE targets: (a) global model, (b) detail of the transition region, (c) detail of the impact zone, (d) detail of the finite element discretization across plies.

with the coefficients specified in Yaghoubi and Liaw[47] was taken. Hard contact pressure-overclosure and metal-laminate friction coefficient $\mu = 0.3$ were used for the projectile–FML interaction. Semiautomatic variable mass scaling with target increment $\Delta t = 10^{-8}$ s was used.

8.12.4.2.2   Results
Two GLARE configurations, namely 2/1 ($[Al/GL_0/GL_{90}]_s$) and 4/3 ($[Al/GL_0/GL_{90}/GL_{90}/GL_0/Al/GL_0/GL_{90}]_s$) layups, were tested. Experimental ballistic curves shown in **Fig. 15** were adapted from data published in Yaghoubi and Liaw.[47] The numerical curves achieved with the modeling strategy described in this chapter fitted with very good agreement the experiments in a wide range of impact velocities. A slight loss of correlation was observed for the 4/3 configuration at impact velocities close to the experimental ballistic limit V_{50} (inherently, a limit value with a 50% perforation probability). Similar deviations of FEM residual velocities were reported by Yaghoubi and Liaw,[47] therefore these results may be associated to the material constants employed for the simulations.

Also in agreement with experiments, projectile erosion was remarkable, as depicted in **Fig. 15**, especially for thick FML. In this particular analysis, the amount of energy invested in the tip blunting phenomenon was not determinant to modify the global response of the impact event beyond the mechanics of the local deformation in target during the plugging. The projectile erosion took place mainly during the first stages of the indentation (**Fig. 16**), as a result of the metal–metal crashing, resulting in a wider contact area of projectile and panel, thus softening the interaction and enlarging the penetration-resistant region of the FML. In a general case, the control of the energy exchange in impacts with crushable projectiles (e.g., the erosion capability of ceramic armours, see Section 8.12.5) can be a valuable design variable to determine the dynamics of the impact event – including changing the projectile trajectory and the failure modes in the target – and to optimize the ballistic performance of shielding panels in future protection systems for vehicles.

The damage mechanisms captured by the model are illustrated in **Fig. 17** for the representative case of GLARE 4/3 with impact velocity $V_i = 250$ m·s^{-1}. Aluminum sheets underwent a mixed deformation mode with predominant shear indentation at the impact face and plastic bending plus membrane-like deformation at the rear face, resulting in petalling and radial crack breakage at full perforation (**Fig. 17(c)**). A pattern of plastic deformation lips in the aluminum layers in conjunction with full interply delamination and severe erosion of fiberglass elements surrounding the projectile orifice was reproduced (**Fig. 17(b)**), in
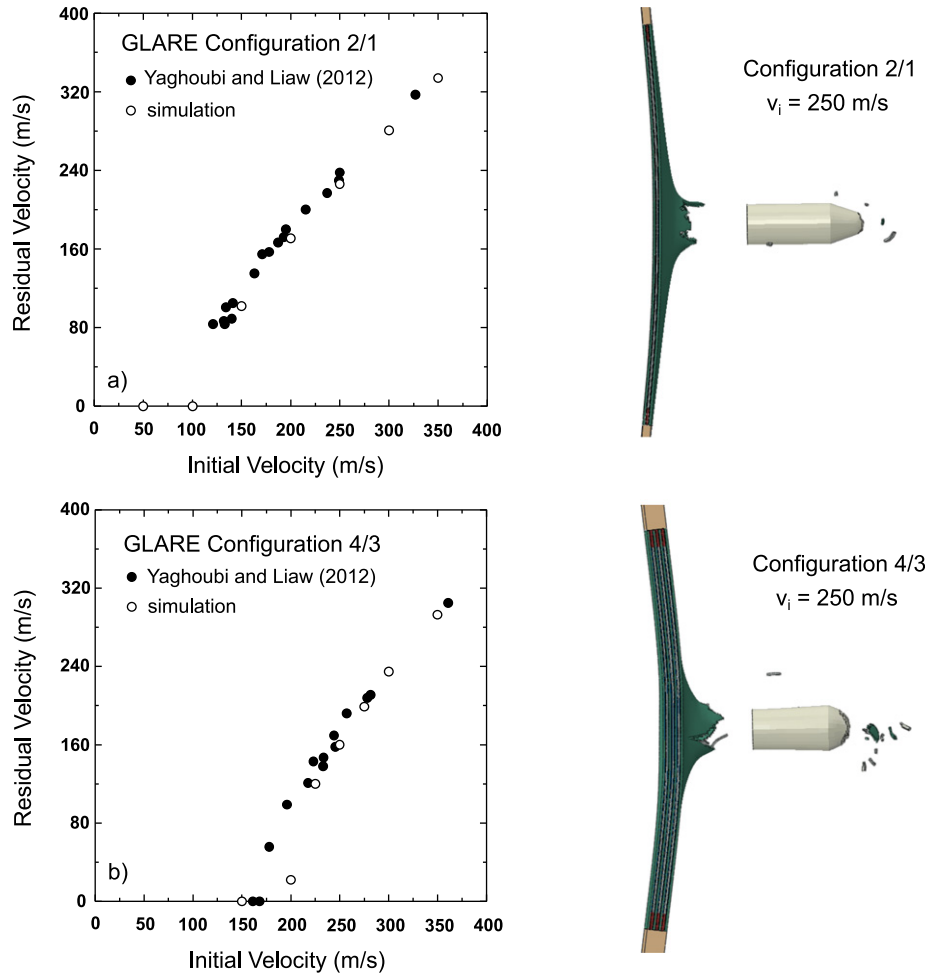
Fig. 15   Comparison of the experimental ballistic curves of GLARE composite panels with the numerical simulations.
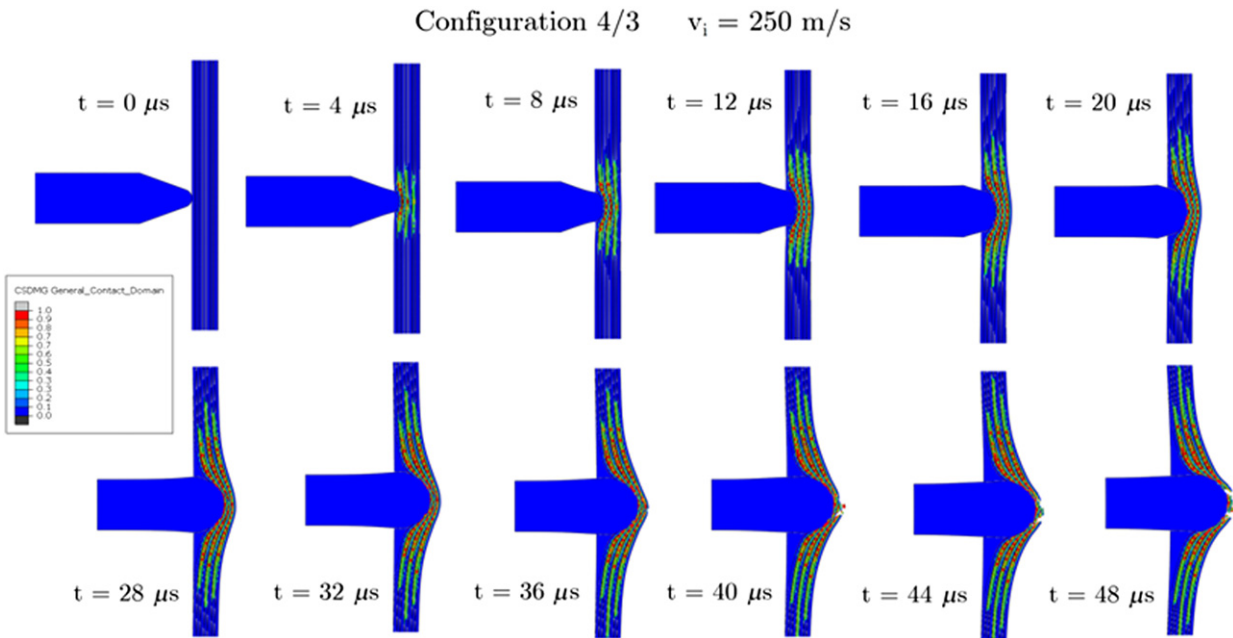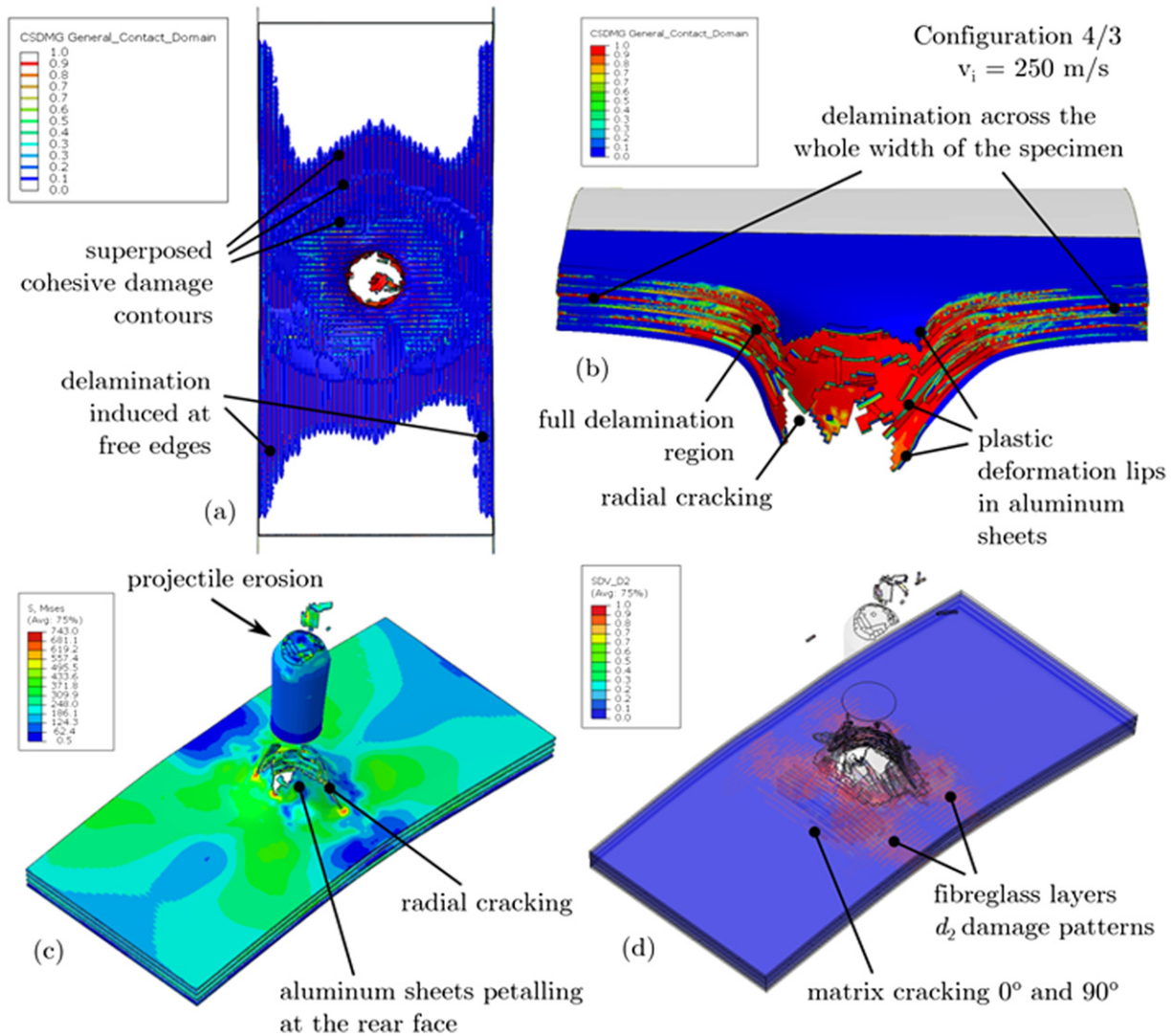

Fig. 16   Snapshots of the projectile penetration in the GLARE composite panel for the configuration 4/3 and $V_i = 250 \, \text{m} \cdot \text{s}^{-1}$.

Fig. 17 Damage mechanisms of the GLARE composite panel configuration 4/3: (a) general delamination area, (b) cross section of the impact area, (c) perforation pattern by petalling, (d) matrix cracking damage variable d_2 in the impact area.

accordance with the experimental results in Yaghoubi and Liaw.[47] Superposed cohesive damage contours of the different interfaces are shown in **Fig. 17(a)**. The influence of the specimen type (beam) was evidenced as a noticeable delamination in bands parallel to the free edges. Due to the $0°/90°$ stacking sequence of the fiberglass plies, the coupled intra/interplay damages were arranged in symmetric patterns regarding the longitudinal and transversal axes of the specimen. A plot of the d_2 damage variable is provided in **Fig. 17(d)**, in which the propagation of matrix cracks along the preferential directions (propagation guided by mesh lines at 0 and $90°$) is illustrated.

8.12.5   Virtual Design of Impact Shields

The numerical tools described previously for monolithic and FML can be used for designing purposes against specific impact threats. In this section, a set of virtual tests simulating the impact event of a metallic fragment against multimaterial laminates is presented, **Fig. 18(a)**. Metallic cylindrical fragments of 75 g were ejected at 469 $m \cdot s^{-1}$ (≈ 8.5 kJ) against 650×275 mm^2 panels. Hybrid solutions containing the use of engineering ceramics (alumina, silicon carbide, and boron carbide), composite laminates (carbon and glass) and dry fabrics (aramid, ultra-high-molecular-weight polyethylene (UHMWPE), or poly(p-phenylene-2, 6-benzobisoxazole) (PBO)), were the most appropriate solutions to sustain high energy impact requirements. The ceramic tiles were used to promote projectile erosion (**Fig. 18(b)**) while distributing the high impact punching load over a wider area reducing the risk of out-of-plane shear tearing. The composite materials were used in multilayer systems to provide a firm support for the ceramic tiles while enabling the appropriate stiffness transition in the through-the-thickness direction to the dry fabrics. Dry fabrics are commonly applied in
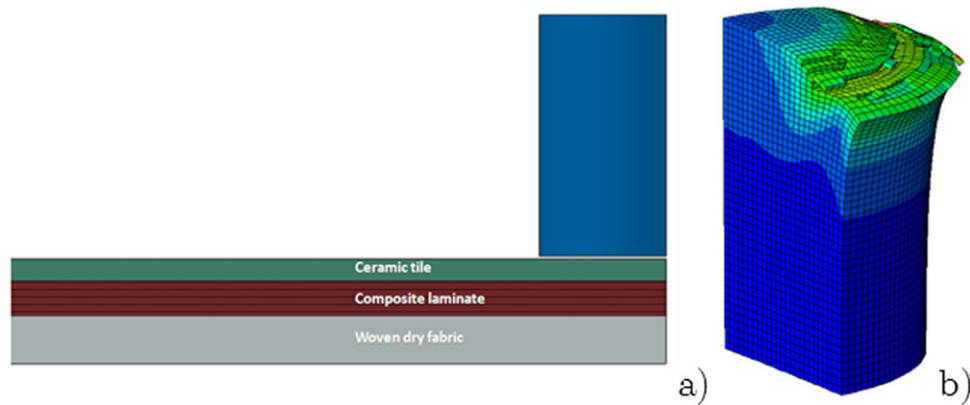
Fig. 18   (a) Multilayer shield configuration containing ceramic tiles, composite laminates, and dry fabrics, (b) Eroded cylindrical projectile.
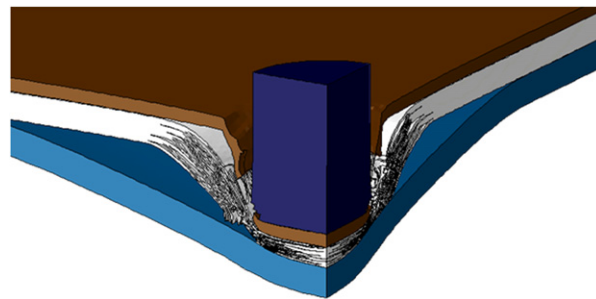
Fig. 19   Multilayer shield configuration subjected to high velocity (HVI) impact showing ceramic fragmentation, composite laminate plugging and membrane deformation of the dry fabrics.

fragment protection systems, armours, bulletproof vests, etc. due to the high strength and energy absorption performances related to their inherent lightness although the efficiency can be limited when they are exposed to irregular fragments with sharp edges.

The mechanical response of the engineering ceramics was modeled with the constitutive material model Johnson–Holmquist (JH2) implemented in Abaqus/Explicit.[49] The constitutive equation consists essentially in three mayor components. First, a representation of the deviatoric strength in both the intact and fully fractured state of the ceramic in the form of a pressure-dependent yield surface. Second, a damage model enabling the transition of the material from the intact to the fractured state. Finally, an equation of state (EOS) for the pressure–density relationship. The mechanical behavior of the composite laminates in the multilayer configurations follows the continuum damage mechanics model presented previously and no further details will be considered in this section.

The mechanical response of the dry fabric panels was modeled using a single reduced integration hexahedron C3D8R element in the thickness direction. The basic idea below this assumption is to treat the dry fabric as a membrane and, therefore, to neglect the bending stiffness during the impact. This assumption is reasonable for the case of a target formed by the stacking of individual dry fabrics without crimping but may be incorrect in the case of thick fabrics highly crimped as in 3D wovens. The model implemented is based on the continuum damage mechanics for anisotropic solids as described in Section 8.12.2.1.2. The elastic compliance matrix of the composite material, Eq. (4), is modified in terms of two damage variables d_1, d_2 which control the evolution of damage in the warp and weft directions along arbitrary loading paths. Only those damage variables associated with the fiber failure are considered in the model and triggered by the in-plane stress tensor of the fabric. It was considered that in-plane compressive and shear stresses in the dry fabric do not cause any damage as the individual yarns buckle under this scenario.

During the first stages of the impact, most of the energy is dissipated by shattering of the ceramic tiles being the energy lost by the projectile work deformation/erosion negligible for this kind of cylindrical geometry, **Fig. 19**. Nevertheless, erosion was observed to contribute, at least, to remove the sharp edges of the projectile in the initial configuration reducing, therefore, the high out-of-plane punching stresses.[50] In a second stage, the composite material starts to fail. Through-the-thickness crushing, fiber breakage and interply delamination play a role during the impact depending on the composite material stacking sequence although shear plugging is the main failure mechanism during this phase. In the last stage of the impact, the energy dissipated corresponds with the strain energy due to the loading of the dry fabric. It should be mentioned that the stiffness gradient in the thickness direction in the multimaterial configuration (ceramic/composite/dry fabric) helps to distribute the impact loads over a wider area of the dry fabric reducing then the sensitivity of these materials to puncture out-of-plane loads. The main drawback of the use of dry fabrics is related with the total deflections required to work in a membrane state and to finally arrest the projectile.

8.12.6   Conclusions and Future Trends

The results showed in the present chapter demonstrated that computational mesomechanics has emerged as a very powerful tool for virtual testing of composite material laminates. The ability of this approach to gather all the physical information regarding the actual deformation and failure mechanisms at the meso level, namely intraply fracture and interply delamination, allowed to establish the relationship between the mechanical properties of the main structural unit, the lamina, and the laminate coupon. These approaches open revolutionary and encouraging opportunities to designers and materials engineers to push composite materials toward their maximum efficiency and performances through a smart combination of physical and virtual tests. Nevertheless, as in other aspects of materials modeling, computational mesomechanics of composite laminates requires further improvements to increase the level of accuracy, robustness of the methodology and reduction of computation times. First, a direct connection of failure mechanisms at the ply level (e.g., matrix cracking, fiber kinking, etc.) with those operating at the fiber/matrix scale should be established by means of computational micromechanics in combination with detailed experiments at the same scale, Llorca et al.[2] Second, the development of alternative computational methods to handle material discontinuities or cracks at the ply level as for instance, kinematic enhancements by extended FE formulations,[51] embedded crack approaches, etc. for those situations not fully covered by the continuum damage mechanics approach and reducing, as much as possible, the effect of the discretization on the predicted results. Finally, the future of composites laminates will require the smart combination of material properties, mechanical and functional, in order to achieve a set of targeted properties for a given application. Structural laminates with energy harvesting and health monitoring capabilities will require the use of advanced materials as carbon nanotubes and graphene fillers.[52]

Acknowledgments

> *See also*: 8.4 Structural Analysis of Composites With Finite Element Codes: An Overview of Commonly Used Computational Methods. 8.11 Foreign Object Impact on Composite Materials and the Modeling Challenges. 8.13 Impact and Mechanical Evaluation of Composite Sandwich Structures. 8.14 Composites Under Dynamic Loads at High Velocities. 8.16 Design of Composite Ballistic Protection Systems

References

1. Llorca, J., González, C., Molina Aldareguía, J.M., Lopes, C.S., 2013. Multiscale modeling of composites: Toward virtual testing … and beyond. JOM: Journal of the Minerals, Metals, and Materials Society 65 (2), 215–225.
2. Llorca, J., González, C., Molina Aldareguía, J.M., Segurado, J., Seltzer, R., et al., 2011. Multiscale modeling of composite materials: A roadmap towards virtual testing. Advanced Materials 23 (44), 5130–5147.
3. Arévalo, E., González, C., Gálvez, F., Llorca, J., 2007. Modelling low velocity impact in c/epoxy laminates. In: Gálvez, F., Sánchez-Gálvez, V. (Eds.), Proceedings of the 23rd International Symposium on Ballistics, vol. 2, Tarragona, Spain, April 16–20, 2007, pp. 1123–1132. Spain: Universidad Politécnica de Madrid.
4. Lopes, C.S., González, C., Falcó, O., et al., 2016. Multiscale virtual testing: The roadmap to efficient design of composites for damage resistance. CEAS Aeronautical Journal 7 (4), 607–619.
5. Falcó, O., Lopes, C., Naya, F., et al., 2017. Modelling and simulation of tow-drop effects arising from the manufacturing of steered-fibre composites. Composites Part A – Applied Science and Manufacturing 93, 59–71.
6. Sádaba, S., Martínez-Hergueta, F., Lopes, C.S., González, C., Llorca, J., 2015. Virtual testing of impact in fiber reinforced laminates. In: Beaumont, P.W.R., Soutis, C., Hozdic, A. (Eds.), Structrual Integrity and Durability of Advanced Composites. Cambridge: Woodhead Publishing, pp. 247–270.
7. Lopes, C.S., Gürdal, Z., Camanho, P.P., Maimí, P., González, E.V., 2009. Simulation of low-velocity impact damage on composite laminates. 50th AIAA/ASME/ASCE/AHS/ASC Structures, Structural Dynamics, and Materials Conference, 4–7 May, 2009, Palm Springs, California.
8. Abrate, S., 1998. Impact on composite structures. Cambridge: Cambridge University Press.
9. Naik, N.K., Shrirao, P., Reddy, B.C.K., 2006. Ballistic impact behaviour of woven fabric composites: Formulation. International Journal of Impact Engineering 32 (9), 1521–1552.
10. Olsson, R., 2000. Mass criterion for wave controlled impact response of composite plates. Composites Part A: Applied Science and Manufacturing 31 (8), 879–887.
11. Dávila, C.G., Camanho, P.P., Rose, C.A., 2005. Failure criteria for FRP laminates. Journal of Composite Materials 39 (4), 323–345.
12. Hashin, Z., 1980. Failure criteria for unidirectional fiber composites. Journal of Applied Mechanics 47 (2), 329–334.
13. Maimí, P., Camanho, P.P., Mayugo, J.A., Dávila, C.G., 2007. A continuum damage model for composite laminates – Part I: Constitutive model. Mechanics of Materials 39 (10), 897–908.
14. Pinho, S.T., Dávila, C.G., Camanho, P.P., Iannucci, L., Robinson, P., 2005. Failure models and criteria for FRP under in-plane or three-dimensional stress states including shear non-linearity. Technical Report NASA/TM-2005-213530. Hampton, VA: NASA, Langley Research Center.
15. Pinho, S.T., Iannucci, L., Robinson, P., 2006. Physically-based failure models and criteria for laminated fibre-reinforced composites with emphasis on fibre kinking: Part I: Development. Composites Part A – Applied Science and Manufacturing 37 (1), 63–73.
16. Puck, A., Schurmann, H., 2002. Failure analysis of FRP laminates by means of physically based phenomenological models. Composites Science and Technology 62 (12–13), 1633–1662.
17. Bažant, Z.P., Oh, B.H., 1983. Crack band theory for fracture of concrete. Materials and Structures 16, 155–157.

18. Turon, A., Dávila, C.G., Camanho, P.P., Costa, J., 2007. An engineering solution for solving mesh size effects in the simulation of delamination with Cohesive Zone Models. Fracture Mechanics 74 (10), 1665–1682.
19. Raimondo, L., Iannucci, L., Robinson, P., Curtis, P.T., 2012. A progressive failure model for mesh-size-independent FE analysis of composite laminates subject to low-velocity impact damage. Composites Science and Technology 72 (5), 624–632.
20. Raimondo, L., Iannucci, L., Robinson, P., Curtis, P.T., 2011. Ballistic impact modelling of composite targets with LS-DYNA3D. 16th International Conference on Composite Structures ICCS 16, Faculty of Engineering, University of Porto (Portugal).
21. Belytschko, T., Lu, Y.Y., Gu, L., 1994. Element-free Galerkin methods. International Journal for Numerical Methods in Engineering 37 (2), 229–256.
22. Johnson, G.R., Cook, W.H., 1985. Fracture characteristics of three metals subjected to various strains, strain rates, temperatures and pressures. Engineering Fracture Mechanics 21 (1), 31–45.
23. Buyuk, M., Kan, S., Loikkanen, M., 2009. Explicit finite-element analysis of 2024-T3/T351 aluminum material under impact loading for airplane engine containment and fragment shielding. ASCE Journal of Aerospace Engineering 22 (3), 287–295.
24. Kay, G., 2003. Failure modeling of titanium 6Al–4V and aluminum 2024-T3 with the Johnson–Cook material model. DOT/FAA/AR-03/57, Technical Report 20591. Washington, D.C.:Office of Aviation Research.
25. Maimí, P., Camanho, P.P., Mayugo, J.A., Dávila, C.G., 2007. A continuum damage model for composite laminates: Part II: Computational implementation and validation. Mechanics of Materials 39 (10), 909–919.
26. Canal, L.P., González, C., Segurado, J., Llorca, J., 2012. Intraply fracture of fiber-reinforced composites: Microscopic mechanisms and modelling. Composite Science and Technology 72 (11), 1223–1232.
27. González, C., Llorca, J., 2007. Mechanical behavior of unidirectional fiber-reinforced polymers under transverse compression: Microscopic mechanisms and modelling. Composite Science and Technology 67 (13), 2795–2806.
28. Naya, F., Lopes, C.S., González, C., LLorca, J., 2015. Computational micromechanics strategies for the analysis of failure in unidirectional composites. In: Camanho, P.P., Hallett, S.R. (Eds.), Numerical Modelling of Failure in Advanced Composite Materials. Woodhead Publishing, pp. 411–433.
29. Naya, F., González, C., Lopes, C.S., van der Veen, S., Pons, F., 2016. Computational micromechanics of the transverse and shear behavior of unidirectional fiber reinforced polymers including environmental effects. Composites Part A: Applied Science and Manufacturing 92, 146–157.
30. Totry, E., González, C., Llorca, J., 2008. Failure locus of fiber-reinforced composites under transverse compression and out-of-plane shear. Composite Science and Technology 68 (3–4), 829–839.
31. Totry, E., González, C., Llorca, J., 2008. Prediction of the failure locus of C/PEEK composites under transverse compression and longitudinal shear through computational micromechanics. Composite Science and Technology 68 (15–16), 3128–3136.
32. Catalanotti, G., Camanho, P.P., Marques, A.T., 2013. Three-dimensional failure criteria for fiber-reinforced laminates. Composite Structures 95, 63–79.
33. Ramberg, W., Osgood, W., 1943. Description of stress–strain curves by three parameters. Technical Note No. 902, National Advisory Committee for Aeronautics.
34. Matzenmiller, A., Lubliner, J., Taylor, R.L., 1995. A constitutive model for anisotropic damage in fiber-composites. Mechanics of Materials 20 (2), 125–152.
35. Herráez, M., Mora, D., Naya, F., et al., 2015. Transverse cracking of cross-ply laminates: A computational micromechanics perspective. Composites Science and Technology 110, 196–204.
36. Camanho, P.P., Dávila, C.G., Pinho, S.T., Iannucci, L., Robinson, P., 2006. Prediction of in situ strengths and matrix cracking in composites under transverse tension and in-plane shear. Composites Part A: Applied Science and Manufacturing 37 (2), 165–176.
37. Jirásek, M., Zimmermann, T., 1998. Analysis of rotating crack model. Journal of Engineering Mechanics 124 (8), 842–851.
38. Jirásek, M., Zimmermann, T., 1998. Rotating crack model with transition to scalar damage. Journal of Engineering Mechanics 124 (3), 277–284.
39. Lopes, C.S., Sádaba, S., González, C., Llorca, J., Camanho, P.P., 2016. Physically-sound simulation of low-velocity impact on fibre reinforced laminates. International Journal of Impact Engineering 92, 3–17.
40. ABAQUS, 2013. v6.13 online documentation, Analysis user's manual 37.1.10. SIMULIA Inc., Dassault Systémes.
41. Guiamatsia, I., Nguyen, G.D., 2014. A thermodynamics-based cohesive model for interface debonding and friction. International Journal of Solids and Structures 51 (3–4), 647–659.
42. Benzeggagh, M.L., Kenane, M., 1996. Measurement of mixed-mode delamination fracture toughness of unidirectional glass/epoxy composites with mixed-mode bending apparatus. Composites Science and Technology 56 (4), 439–449.
43. Sebaey, T.A., Blanco, N., Costa, J., Lopes, C.S., 2012. Characterization of crack propagation in mode I delamination for multidirectional CFRP laminates. Composites Science and Technology 72 (11), 1251–1256.
44. Schön, J., 2012. Coefficient of friction of composite delamination surfaces. Wear 237 (1), 77–89.
45. Godwin, W., Davies, G.A.O., 1988. Impact behaviour of thermoplastic composites. Proceedings of the International Conference Computer aided design in composite material technology. pp. 371–382.
46. Pernas-Sánchez, J., Artero-Guerrero, J.A., Zahr Viñuela, J., Varas, D., López-Puente, J., 2014. Numerical analysis of high velocity impacts on unidirectional laminates. Composite Structures 107, 629–634.
47. Yaghoubi, A.S., Liaw, B., 2012. Thickness influence on ballistic impact behaviors of GLARE 5 fiber–metal laminated beams: Experimental and numerical studies. Composite Structures 94 (8), 2585–2598.
48. van der Meer, F.P., Sluys, L.J., 2010. Mesh-independent modeling of both distributed and discrete matrix cracking in interaction with delamination in composites. Engineering Fracture Mechanics 77 (4), 719–735.
49. Holmquist, T.J., Templeton, D.W., Bishnoi, K.D., 2001. Constitutive modeling of aluminum nitride for large strain, high-strain rate, and high-pressure applications. International Journal of Impact Engineering 25 (3), 211–231.
50. Bürger, D., Rocha de Faria, A., de Almeida, S.F.M., de Melo, F.C.L., Donadon, M.V., 2012. Ballistic impact simulation of an armour-piercing projectile on hybrid ceramic/fiber reinforced composite armours. International Journal of Impact Engineering 43, 63–77.
51. Sádaba, S., Romero, I., González, C., Llorca, J., 2015. A stable X-FEM in cohesive transition from closed to open crack. International Journal for Numerical Methods in Engineering 101 (7), 540–570.
52. Senokos, E., Reguero, V., Palma, J., Vilatela, J.J., Marcilla, R., 2016. Macroscopic fibres of CNTs as electrodes for multifunctional electric double layer capacitors: From quantum capacitance to device performance. Nanoscale 8, 3620–3628.

Relevant Websites

http://www.materiales.imdea.org/
    IMDEA Materials Institute.
http://www.materiales.imdea.org/groups/cm/
    IMDEA Materials Institute Composite Materials Group.